



Using machine learning for real-time estimates of snow water equivalent in the watersheds of Afghanistan

Edward H. Bair¹, Andre Abreu Calfa^{2,a}, Karl Rittger³, and Jeff Dozier⁴

¹Earth Research Institute, University of California, Santa Barbara, CA 93106-3060, USA

²Department of Computer Science, University of California, Santa Barbara, CA 93106-5110, USA

³National Snow and Ice Data Center, University of Colorado, Boulder, CO 80309-0449, USA

⁴Bren School of Environmental Science and Management, University of California, Santa Barbara, CA 93106-5131, USA

^anow at: Arista Networks, Santa Clara CA 95054, USA

Correspondence: Edward H. Bair (nbair@eri.ucsb.edu)

Received: 5 September 2017 – Discussion started: 11 October 2017

Revised: 29 March 2018 – Accepted: 3 April 2018 – Published: 3 May 2018

Abstract. In the mountains, snowmelt often provides most of the runoff. Operational estimates use imagery from optical and passive microwave sensors, but each has its limitations. An accurate approach, which we validate in Afghanistan and the Sierra Nevada USA, reconstructs spatially distributed snow water equivalent (SWE) by calculating snowmelt backward from a remotely sensed date of disappearance. However, reconstructed SWE estimates are available only retrospectively; they do not provide a forecast. To estimate SWE throughout the snowmelt season, we consider physiographic and remotely sensed information as predictors and reconstructed SWE as the target. The period of analysis matches the AMSR-E radiometer's lifetime from 2003 to 2011, for the months of April through June. The spatial resolution of the predictions is 3.125 km, to match the resolution of a microwave brightness temperature product. Two machine learning techniques – bagged regression trees and feed-forward neural networks – produced similar mean results, with 0–14 % bias and 46–48 mm RMSE on average. Nash–Sutcliffe efficiencies averaged 0.68 for all years. Daily SWE climatology and fractional snow-covered area are the most important predictors. We conclude that these methods can accurately estimate SWE during the snow season in remote mountains, and thereby provide an independent estimate to forecast runoff and validate other methods to assess the snow resource.

1 Introduction

Accurate estimates of snow water equivalent (SWE) in mountain watersheds pose a longstanding, unsolved problem. Lettenmaier et al. (2015) note that “retrieval of snow water equivalent from space remains elusive especially in mountain areas” and argue that “this area deserves more strategic thinking from the hydrology community.” Dozier et al. (2016) identify five approaches to the problem, but point out that all are problematic in some way. Operational models' high uncertainty imposes costs for water users. For instance, April to July runoff forecasts in the well instrumented American River Basin, in California's Sierra Nevada, have a median error of 18 % and a 90th percentile error (1 year out of 10) exceeding 60 % (Dozier, 2011). Uncertainty stems from the heterogeneous distribution of mountain snow. A sparse network of sensors sometimes fails to characterize this heterogeneity or even its integrated volume over a drainage basin. In Afghanistan, few stations measure any hydrological or meteorological variables, and only a few dams store snowmelt runoff. Low snowpack years lead to humanitarian crises with little warning, as rivers and streams run dry in the fall and crops fail (e.g., USAID, 2008).

Remotely sensing SWE in the mountains has also proven difficult. Passive microwave (PM) sensors offer real-time global SWE estimates but suffer from several issues, notably signal loss in wet snow (Li, 2006), saturation in deep snow (Hancock et al., 2013; Kelly et al., 2003; Takala et al., 2011; Tedesco and Narvekar, 2010), decreasing SWE

Table 1. Climate records (monthly averages) from Kabul and Salang Pass.

Month	Mean air temp., °C	Mean precip., mm	Max snow depth, cm	Mean days with snow	Mean air temp., °C	Mean precip., mm	Max snow depth, cm	Mean days with snow
Kabul, 1791 m (1956–1983)					North Salang, 3366 m (1960–1983)			
January	−2.3	34.3	48	7	−10.3	108.7	300	13
February	−0.7	60.1	65	6	−9.5	142	367	15
March	6.3	67.9	30	3	−5.4	185.9	383	18
April	12.8	71.9	0	0	−0.1	197.8	450	15
May	17.3	23.4	0	0	2.9	123.7	366	10
June	22.8	1	0	0	7.5	10	66	1
July	25	6.2	0	0	9.7	6.8	0	0
August	24.1	1.6	0	0	8.6	6.7	2	0
September	19.7	1.7	0	0	4.7	7.5	40	1
October	13.1	3.7	0	0	0.7	30.2	102	6
November	5.9	18.6	4	0	−4	68.4	184	8
December	0.6	21.6	30	4	−7.8	104.3	320	11
Annual	12.05	312	14.75	2	−0.25	992	215	8

with increasing forest fraction (Nolin, 2010; Tedesco and Narvekar, 2010), subpixel variability in the mountains owing to the large (~ 25 km) pixel size (Vander Jagt et al., 2013), and SWE overestimation in the presence of large grains, such as depth and surface hoar (Derksen et al., 2005; Durand et al., 2011). A new product, the Calibrated Passive Microwave Daily EASE-Grid 2.0 Brightness Temperature Earth System Data Record (hereafter referred to as enhanced resolution PM, Brodzik and Long, 2016) addresses the resolution limitation by providing gridded brightness temperatures at 3.125 km or coarser spatial resolution by taking advantage of overlapping footprints, at the expense of some added noise. Even given these concerns, PM sensors could, in principle, provide less biased information if integrated with other datasets. Doing so requires an independent method of estimating spatially distributed SWE.

A strong candidate for such an independent estimate is reconstructed SWE. From satellite-based imagery in the visible through shortwave infrared bands, we can successfully map fractional snow-covered area (F_{SCA}) at sub-pixel resolution (Painter et al., 2009; Rittger et al., 2013; Rosenthal and Dozier, 1996). From the remotely sensed date of disappearance, snowmelt can be calculated backward to reconstruct SWE for each day back to peak accumulation (Martinec and Rango, 1981). Successful examples of reconstructed SWE include large basins in the Rocky Mountains (Molotch, 2009; Schneider and Molotch, 2016) and the Sierra Nevada (Giroto et al., 2014; Guan et al., 2013; Rittger et al., 2016). When compared with SWE estimates from NASA's Airborne Snow Observatory in the upper Tuolumne River Basin from 2013 through 2015, reconstructed SWE estimates had a 26 % mean absolute error (MAE, Bair et al., 2016) and no bias. In contrast, the Snow Data Assimilation System (SNODAS, Barrett, 2003), the operational model used by the US National Weather Service, had a 65 % MAE and overestimated

snow every year in that analysis. Reconstruction's main advantage lies in its provision of spatially resolved SWE estimates without the need for ground-based observations. Reconstruction's biggest disadvantage is that SWE can only be calculated retroactively after snow disappears, and it works best in areas with clear accumulation and ablation periods. It also cannot assess SWE in the accumulation zones of glaciers, and the capability of current methods of mapping F_{SCA} on the ablation zones of glaciers has not been assessed (Painter et al., 2012b).

By nature, space-time cubes of retrievals and derived products from satellites are “big data.” For this type of information, machine learning has proven particularly effective compared to traditional multivariate statistical techniques. Machine learning techniques such as ensemble regression (Breiman, 2001; Hastie et al., 2009) and neural networks (Hagan et al., 2014) are able to reproduce nonlinear effects and interactions between variables without assumptions of a functional form. These machine learning techniques are also robust to overfitting in the presence of large datasets.

The goal of this study is to develop and evaluate models using machine learning for SWE prediction in Afghanistan's watersheds. Predictors include static and dynamic variables that are available in near-real time, during the snow season rather than after the snow has melted. The target variable is reconstructed SWE, which we suggest is the closest ground-truth available for data-sparse regions.

2 Study area

Afghanistan's main mountain range, the Hindu Kush (Fig. 1), is marked by seasonal drought during the summer and fall. Salang Pass, which straddles the Upper Kabul and Amu Darya watersheds, is the only location in Afghanistan above

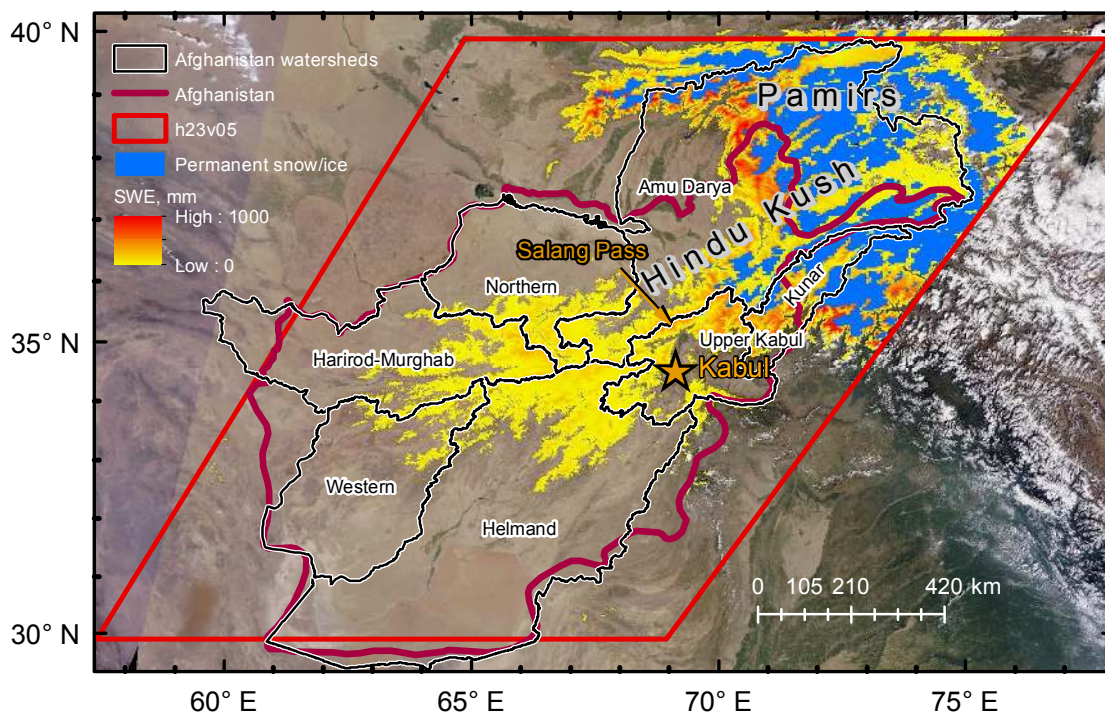


Figure 1. MODIS true color image of snow covered watersheds of Afghanistan with 2003–2011 1 April reconstructed mean SWE overlaid. Also shown are the watersheds of Afghanistan (from Daly et al., 2012), the country outline, the h23v05 MODIS tile, and areas with permanent snow and ice.

3000 m with long term (albeit not current) climate records (Table 1). Snow depth peaks here in April at a maximum of 450 cm and melts out by July. In comparison, snow depth in Kabul peaks in February at a maximum of 65 cm and melts out by April. The highest peaks in Afghanistan at 7500 m are covered by permanent snow and ice. Historically, about 5 % of the country's land area was forested. Decades of war, illegal logging, and a lack of replanting have reduced forest cover to only 2 % (United Nations, 2009). The limited forest cover facilitates remote sensing of the snowpack from optical and microwave instruments, as canopy cover obstructs the view for optical instruments (Raleigh et al., 2013) and interferes with passive microwave emission (Tedesco and Narvekar, 2010). Because of its seasonal summer drought and lack of reservoirs, Afghanistan's water supply is particularly susceptible to year-to-year variations in snowfall.

3 Methods

3.1 Predictors and target

A mix of static physiographic (Fassnacht et al., 2012) and dynamic variables were used as predictors (Table 2). All variables were computed at or resampled to 3.125 km resolution using Gaussian pyramid reduction or expansion (Burt and Adelson, 1983) for the initial steps and bilinear interpola-

tion for the final step. The 3.125 km resolution was chosen because it is the finest resolution available for the 36 GHz enhanced resolution PM brightness temperature. The study area shown in Fig. 1 is the MODIS h23v05 tile, which the snow-covered portions of Afghanistan's watersheds fit into. Elevation dependent variables were calculated from the 30 arcsec ASTER digital elevation model.

Only nighttime data from the microwave brightness temperatures were used, to almost always image a frozen snowpack. The time of acquisition for the brightness temperatures varies by up to 30 min centered around 01:00 A.M. local Afghanistan time. The 36 GHz V (vertical polarization) brightness temperatures are available at 3.125 km, but the 18 GHz V brightness temperatures are available only at a resolution of 6.25 km, so the 18 GHz brightness temperatures were resampled to the 3.125 km resolution. Likewise, the 10 GHz brightness temperatures are available only at 12.5 km resolution, so they were also resampled to 3.125 km. Two different brightness temperature differences ($T_{18V}-T_{36V}$ and $T_{10V}-T_{18V}$) were used to account for shallow and deep snow. Use of these three brightness temperature channels in simulations has shown promise for SWE retrievals (Markus et al., 2006), although the $T_{18V}-T_{36V}$ is more commonly used (e.g., Kelly, 2009). At the latitude of the Afghanistan, AMSR-E has 2-day repeat coverage, so gaps in brightness temperatures were filled using bilinear interpolation. The brightness tem-

peratures were then smoothed using a 7-day moving median filter. The F_{SCA} and SWE dynamic variables are discussed below.

3.2 Reconstruction using the ParBal energy balance model

To compute snow and ice melt, we used the ParBal (Parallel Energy Balance) Model (Bair et al., 2016), a full energy balance snow and ice melt model, run at an hourly timestep and initially at 463 m resolution in a MODIS sinusoidal projection. ParBal, unlike most melt models, does not require total precipitation, the most uncertain term in the water budget for montane areas (Adam et al., 2006; Milly and Dunne, 2002). At any time step j , the snow melt M_j is a product of the fractional snow covered area F_{SCA} and the potential melt M_p , i.e., the melt if a pixel were 100 % snow covered (Molotch and Bales, 2005):

$$M_j = F_{\text{SCA},j} \times M_{p,j}. \quad (1)$$

The potential melt is computed using downscaled inputs from reanalysis and remotely sensed data. We briefly summarize this process and refer the reader to Bair et al. (2016) for details. Elevation dependent variables are scaled using the difference between a coarse-resolution digital elevation model (DEM) for CERES (Clouds and the Earth's Radiant Energy System, Rutan et al., 2015) or GLDAS (Global Land Data Assimilation System, Rodell et al., 2004) and a DEM at the 463 m scale. CERES incoming solar radiation is used to derive the transmissivity, then the local illumination conditions are computed using horizon angles and knowledge of the sun's position. For incoming longwave radiation, a sky view factor (Dozier and Frew, 1990) is used. Latent and sensible fluxes are computed using exchange coefficients that depend on wind speed. Melt can only occur when the snow surface temperature is at 0 °C. Cold content is accounted for to prevent spurious melt when the energy balance is positive, but the snowpack bulk (not surface) temperature is well below the melting temperature. Incoming radiative fluxes and other meteorological variables are from GLDAS and CERES.

3.2.1 Inputs to ParBal

Dynamic inputs to ParBal to compute snow and ice melt include F_{SCA} , snow albedo, incoming solar radiation, incoming longwave radiation, air temperature, wind speed, and specific humidity. Downscaled forcings from GLDAS at 1/4° and CERES-SYN at 1° provided all the energy inputs. By using both GLDAS and CERES, we overcome biases from failures to detect clouds in the shortwave and longwave GLDAS and NLDAS (Cosgrove et al., 2003) products (Bair et al., 2016; Hinkelman et al., 2015; Lapo et al., 2017). Specifically, CERES SYN provided incoming shortwave and longwave

fluxes while GLDAS provided air temperature, wind speed, and specific humidity. Note that GLDAS only provides wind speed, not its vector, therefore the terrain-based downscaling approach (Liston and Elder, 2006; Liston et al., 2007) that Bair et al. (2016) used could not be applied. Instead, GLDAS wind speeds were resampled from 1/4° to 463 m. Although this resampling leads to errors in wind speeds and is a source of uncertainty, the latent and sensible terms that depend on wind speed tend to be small and usually of opposite sign (Marks and Dozier, 1992). GLDAS and CERES were linearly interpolated from 3 to 1 h intervals to match the model time step.

Key inputs are the remotely sensed F_{SCA} and snow albedo. We use the products MODIS Snow Covered Area And Grain size (MODSCAG, Painter et al., 2009) along with the MODIS Dust and Radiative Forcing in Snow (MOD-DRFS, Painter et al., 2012a). Snow uncontaminated by particulates is rare outside Antarctica (Warren and Wiscombe, 1980), therefore the clean snow albedo estimate from MODSCAG is adjusted for impurities. We then gap fill and smooth these snow property retrievals using a validated algorithm (Dozier et al., 2008; Rittger et al., 2013). The use of a remotely sensed albedo, to which snowmelt is very sensitive, has been shown to be far more accurate (Bair et al., 2016; Molotch and Bales, 2006) than age-based schemes (Malik et al., 2014; U.S. Army Corps of Engineers, 1956), yet these age-based schemes predominate in snow models (Giroto et al., 2014; Margulis et al., 2015; Markstrom et al., 2015; Molotch, 2009). To compensate for sensitivity of modeled snowmelt to albedo, some SWE reconstruction studies (Guan et al., 2013; Molotch, 2009; Molotch and Margulis, 2008) used ground-based ancillary information to find the occurrence date of snowfall.

Static inputs to ParBal to compute snow and ice melt include: elevations, slopes and azimuths, horizon angles, topographic view factors, and canopy cover. For elevation data, we use ASTER GDEM version 2. Slopes, azimuths, horizon angles, and view factors were then computed from the digital elevation models (Dozier and Frew, 1990). Canopy type and fraction were taken from the Global Land Survey (USGS, 2009).

Table 2. Predictor and target variables.

Name	Description
Physiographic predictors	
Day of year	Sine of day of year; sine function used to create a continuous variable.
Elevation	Pixel average elevation
Latitude	Pixel center latitude
Longitude	Pixel center longitude
Northwest/west/southwest barrier difference	Elevation difference between pixel and highest pixel in each direction, also called shield height.
West/southwest distance to ocean	Pixel distance to ocean or sea in each direction.
Southness	Northwest was not used, as distance exceeds 5000 km for many pixels. Computed as $\sin(\text{slope}) \times \cos(\text{aspect})$, with slope as upward from horizontal and aspects from south with counter-clockwise as positive (Dozier and Frew, 1990).
Dynamic predictors	
TB _{10V} –TB _{18V}	Difference between enhanced resolution PM brightness temperature at 10 GHz, vertically polarized, and 18 GHz, vertically polarized.
TB _{18V} –TB _{36V}	Difference between enhanced resolution PM brightness temperature at 18 GHz, vertically polarized, and 36 GHz, vertically polarized.
F_{SCA}	Fractional snow-covered area
Mean reconstructed SWE	Mean daily SWE computed over all years except the target year
Target	
Reconstructed SWE	Reconstructed daily SWE

3.2.2 Cold content

To limit early melt, ParBal constrains melt to only occur in a ripe snowpack. In earlier versions, cold content did not need to be accounted for since the model was not run prior to peak SWE. Cold content is not directly modeled since the density and depth of the snowpack are not known. Instead, calculating its proxy uses a scheme modified from Jepsen et al. (2012).

$$M_{p,j} = \max \left(0, \min \left[\sum_{k=0}^j Q_{\text{net},k}, Q_{\text{net},j} \right] \right). \quad (2)$$

Q_{net} is the sum of the following energy balance terms:

$$Q_{\text{net},j} = R_j + H_j + L_j + G_j, \quad (3)$$

where R is net radiation, H and L are sensible and latent heat exchanges, and G is conduction, all at time step j . In the Jepsen et al. (2012) approach, cold content is reset daily at midnight ($k = 0$ in Eq. 2). Our modification is to reset the cold content daily after sunset, which is a more accurate estimate of when the energy balance becomes negative and daily cold content starts building. Comparisons of melt from ParBal constrained with this cold content scheme and lysimeter measurements at an energy balance site on Mammoth Mountain, CA (Bair et al., 2015) show excellent agreement (Fig. S1 in the Supplement) with both the onset of melt

that reached the bottom of the snowpack and seasonal cumulative total melt. Complex routing through the snowpack before reaching the lysimeters likely causes a few discrepancies in the quantities of daily melt (Kattelmann, 2000; Wever et al., 2014).

3.3 Validation in California's Sierra Nevada

To better understand the biases and errors in our reconstructed SWE estimates used in Afghanistan, we ran ParBal in the Sierra Nevada as it was run in Afghanistan. Specifically, as explained in Sect. 3.2.1, meteorological forcings from GLDAS at $1/4^\circ$ spatial resolution and radiometric forcings from CERES at 1° spatial resolution were used. For validation, we used three years of the best spatial SWE estimates available from NASA's Airborne Snow Observatory for the Upper Tuolumne River Basin in the Sierra Nevada. For comparison, the Supplement includes published reconstructions from ParBal forced with National Land Data Assimilation System 2 (Xia et al., 2012) at $1/8^\circ$ spatial resolution (Bair et al., 2016). F_{SCA} was the same for both GLDAS/CERES and NLDAS model runs, which Bair et al. (2016) showed to have 15 % MAE and 5 % bias on average. Cold content was included in the GLDAS/CERES run, but not the NLDAS run.

Figure S2 and Tables S1 and S2 show full results of the two model runs, which are summarized here. Overall, compared to the NLDAS model run, MAE in the GLDAS/CERES run from peak SWE through melt out decreased from 26 to 22 %, and

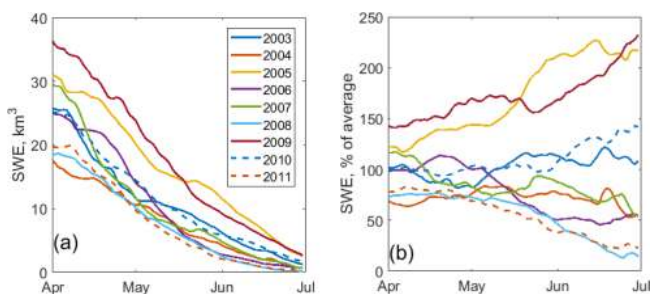


Figure 2. Reconstructed total SWE volume (a) and percent of 2003–2011 average (b) for all non-glacierized pixels in the study area.

but at the expense of some bias which dropped from 0 to -8% . Notably, the GLDAS/CERES model run was slightly more accurate (16 and 19 % MAE for 2014 and 2015 vs. 20 and 31 % MAE) than the NLDAS model run in 2014 and 2015, both drought years with SWE depths similar to what we expect in Afghanistan. Also of note is that for the areas with low canopy cover (0 to 0.2), similar to much of the snow-covered areas in Afghanistan, the GLDAS/CERES model run showed a -19% bias, compared to a 12 % bias in the NLDAS model run. Full analysis of the biases and model sensitivity is beyond the scope of this study. For the purposes of this study, we conclude that the reconstructed SWE estimates using the GLDAS/CERES forcings show similar accuracy to the reconstructed SWE using NLDAS forcings.

3.4 Validation in Afghanistan

Examination and validation of reconstructed SWE (Fig. 2a, b) shows absolute and relative ablation curves for all non-glacierized pixels. The interannual variability is high, with a difference of about $2\times$ in peak SWE between the wettest year (2009) and the driest year (2004). Expressed relative to the mean, the peak SWE was 140 % in 2009 vs. 70 % in 2004. Especially later in the melt season, some years show values in excess of 200 % of the mean while others show values less than 25 % of the mean (Fig. 2b).

To our knowledge, there are too few in situ measurements of SWE in Afghanistan during the 2003 to 2011 study period to compare with reconstructed SWE. Instead, we used passive microwave-based SWE estimates from AMSR-E from a previous study (Daly et al., 2012); Table 3 shows comparisons of SWE on 1 April.

The Amu Darya and the Kunar basins were excluded because of extensive glaciers, such that passive microwave estimates of SWE do not provide meaningful estimates of snow on the ground. In every basin on 1 April, there were many areas with more reconstructed SWE than the passive microwave saturation limit of 150 mm (Hancock et al., 2013; Kelly et al., 2003; Takala et al., 2011; Tedesco and Narvekar, 2010). Basin wide, differences between the results of this study and the results reported in Daly et al. (2012) were

small, < 8 mm, for all basins except the Upper Kabul (22 mm difference), which had the highest average SWE in both studies.

At North Salang or Salang Pass, the only high elevation station with long-term climatological measurements available in Afghanistan (Table 1), the October–May precipitation is 961 mm. October to May corresponds to the time when most of the precipitation falls as snow, based on the mean temperature. Using an energy balance model, Schulz and de Jong (2004) estimate that on average 44 % of the snowpack sublimated in the climatologically similar Atlas Mountains of Morocco. Likewise, Bair et al. (2015) also estimate that on average 44 % of the snowpack sublimated at a high altitude site in California’s Sierra Nevada using co-incident lysimeters and a snow pillow. Using this sublimation estimate leaves 538 mm of SWE at the peak, assuming negligible mass gain from condensation and deposition. The mean 1 April reconstructed SWE, which can be assumed to be close to the peak, for Salang Pass is 498 mm.

Since 1983, when weather stations in Afghanistan stopped submitting measurements to the World Meteorological Organization (e.g., Table 1), there have been no in situ snow measurements accessible within the country, at least to the authors of this study. In 2015, this changed when FOCUS Humanitarian Assistance, which is now referred to as the Aga Khan Agency for Habitat (AKAH), established 82 Weather Monitoring Posts, hereafter called stations, in Afghanistan, Pakistan, and Tajikistan (Chabot and Kaba, 2016). These stations were established for aid in operational avalanche forecasting as a response to widespread and deadly avalanche cycles that occur often in these countries, but were especially catastrophic in 2012 and 2015. In the fall of 2016, we submitted a request to AKAH for access to a central database of measurements from these stations. Our request was granted a year later. Digital records only go back to the fall of 2016, but are available for 96 stations, and 88 stations recorded measurable snow on the ground (Fig. 3). The snow measurements are all manual and include new (24 h) snow and total snow depth. Maximum and minimum daily temperature, wind speed and direction, and 24 h manual rainfall were also recorded.

Although measurements from the stations do not cover our 2003–2011 study period, they are a unique validation source in a region where snow measurements are otherwise nonexistent. Therefore, we ran reconstructed the WY 2017 snowpack with ParBal for the h23v05 tile and validated our SWE estimates using the station snow measurements.

For quality control, we applied an outlier filter (Hampel, 1974) to the time series of snow depth for each station. Time series were then plotted for each station and spurious values (particularly zeros surrounded by high values that were not caught by the automated filter) were manually removed. Of the 96 stations, 15 had snow depth time series that were too erratic or missing too many values for scientific use. Measurements from these 15 stations were discarded.

Table 3. Basin area and 1 April reconstructed mean basin-wide SWE estimates from this study compared to passive microwave (AMSR-E) estimates from Daly et al. (2012). Highly glacierized basins are excluded.

	Years compared	Helmand	Western	Harirod-Murghab	Upper Kabul	Northern
Basin area, km ²	–	226 580	85 289	90 036	42 159	70 910
SWE, mm, this study	2003–2011	7	1	13	61	12
SWE, mm, Daly et al. (2012)	2002–2010	11	4	15	43	20

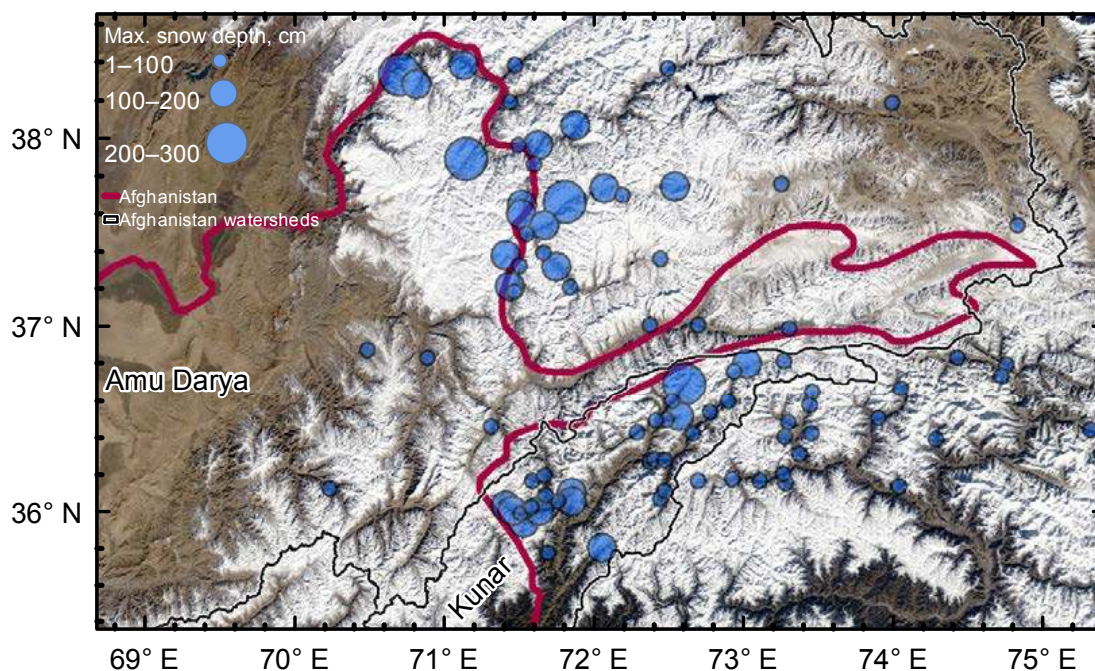


Figure 3. Maximum snow depth from WY 2017 manual measurements at AKAH stations in Afghanistan, Pakistan, and Tajikistan overlaid on a MODIS true color image.

For the remaining 81 stations, the snow depth estimates were transformed to SWE using a snow climate classification (Sturm et al., 1995) and associated density model (Sturm et al., 2010). For each station, the November–March daily mean temperature was used to calculate cooling degree months (CDM). The 24 h new snow and rainfall observations were used to estimate the daily precipitation P , with the simplified assumption of 100 kg m^{-3} density new snow. Wind speed at the time of observation was used as a daily wind speed since 24 h average wind speeds were not available. The CDM were combined with November–March mean daily precipitation (\bar{P}) and mean daily wind speed (\bar{WS}) and feed through a classification tree (Fig. 8 in Sturm et al., 1995) to determine the snow climate. Boundary values used were: 125°C for CDM; 2 mm day^{-1} for \bar{P} ; and 1.25 m sec^{-1} for \bar{WS} .

Even though some of these stations were over 3000 m in elevation, they tended to have relatively warm (around melting) November–March mean air temperatures, so they all classified in the warm snow types: alpine, maritime, and prairie (Fig. 4).

Of those three classifications, alpine was predominant ($N = 49$), characterized by low precipitation and low wind speed. Some of the stations with heavier precipitation classified as maritime ($N = 14$) which is slightly misleading given that they are several thousand km from an ocean or sea. Prairie was the least common ($N = 11$), classified by warm temperatures, low precipitation, and high winds. A few of the stations ($N = 7$) were missing more than 10 observation dates for a given month from November–March, so they were not classified. Instead, we set those stations to alpine, the modal value. Also, after classification, we noticed that some of the prairie stations had high peak snow depths ($> 50 \text{ cm}$). We suspect that the new snow was not being consistently or accurately recorded for these stations, so we set those prairie stations to the modal snow class (alpine).

With the snow climate determined, a snow density model (Eq. 6 in Sturm et al., 2010) was used to estimate the bulk density of the snowpack. The density model coefficients (Table 4 in Sturm et al., 2010) vary with snow climate. Expected relative SWE bias from this model based on validation from

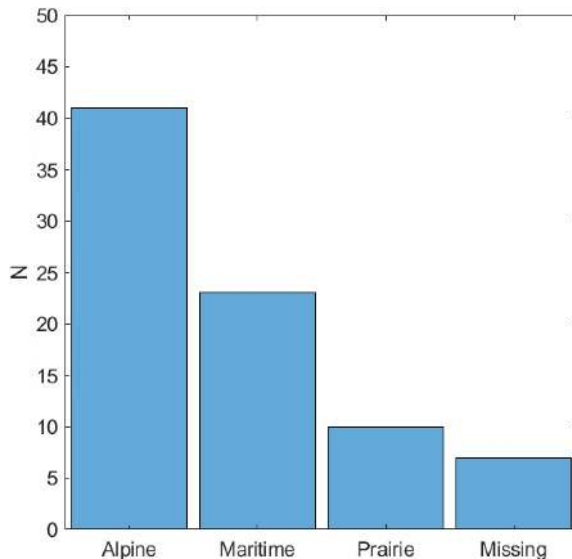


Figure 4. Snow climate classes for 81 AKAH stations.

alpine and maritime areas is -12 to $+26$ % of SWE (Sturm et al., 2010).

The bulk density was used to estimate SWE for each station. Reconstructed SWE values (modeled) were then compared with this SWE estimate from snow depth (measured). For comparison, we assume the MOD09GA gridded product, from which our F_{SCA} estimates are based, has a geolocational uncertainty of 0.5 – 1.0 pixel (250 – 500 m), depending on the sensor angle (Tan et al., 2006; Xiaoxiong et al., 2005). Thus, we examined the closest pixel to each station, as well as the 8 neighbors surrounding that pixel. For each of those 9 pixels, we further assumed that the SWE at each station could vary from 88 to 126 % of the value calculated with the density model. We refer to these variations in location and density as uncertainty. Taking into account the geolocational and density model uncertainties, we chose the reconstructed SWE that most closely matched the computed value at each station, adjusted each for both sources of uncertainty.

For three selected dates, the agreement between modeled and measured values is excellent (Fig. 5). These dates were selected to approximate peak SWE for most of the stations. Mean absolute error (MAE) is 7 – 18 mm and the bias, relative to the measured mean value, is -3 to $+4$ %. For all stations for all dates (March to May), modeled results are unbiased with an MAE of 5 mm (13 %).

We also examined the time series from March to May for 9 stations with deeper snowpacks (> 100 mm SWE on 1 March). Plotted are stations with negative bias (Fig. 6a–c), no bias (Fig. 6d–f), and high bias (Fig. 6g–i). Maximum negative bias is -113 mm (-12 %) for Ruah (Fig. 6a). Maximum positive bias is 76 mm (26 %) for Arakht (Fig. 6i).

Picking the best match from a 9-pixel neighborhood with a -12 to 26 % adjustment for density uncertainty is a best-case

Table 4. Error statistics for selected dates and different ways to account for uncertainty. See Sect. 3.4 for details.

	MAE, mm	MAE, %	Bias, mm	Bias, %
Neighborhood and density uncertainty				
1 March	18	11 %	−4	−2 %
15 March	16	14 %	5	4 %
1 April	7	13 %	−1	−2 %
Neighborhood uncertainty only				
1 March	85	53 %	−7	−4 %
15 March	81	70 %	21	18 %
1 April	55	104 %	−28	−53 %
Density uncertainty only				
1 March	23	14 %	−5	−3 %
15 March	18	16 %	3	3 %
1 April	8	15 %	−3	−6 %
No uncertainty				
1 March	75	47 %	−5	−3 %
15 March	88	77 %	47	41 %
1 April	54	102 %	0	0 %

scenario. To bound our errors, we also matched our modeled SWE values using three other scenarios that show higher errors: (a) 9-pixel neighborhood, but with no adjustment for density uncertainty; (b) an adjustment for density uncertainty but no use of a neighborhood; and (c) no use of a neighborhood and no density adjustment.

Examination of all 4 scenarios shows that the uncertainty in density is the largest source of error, as the inclusion of a neighborhood with uncertainty in density barely improves the error statistics (Table 4). In relative terms, the MAE ranges from 14 to 102 % and the bias ranges from -53 to $+41$ % when one of more sources of uncertainty are not accounted for. These uncertainties are inherent when using snow depth point measurements to verify SWE estimates for 0.5 km pixels. The finding that uncertainty in density accounts for most of the error only reaffirms the need for in situ SWE measurements in the region. Nonetheless, these AKAH measurements are the only in situ snow measurements accessible to us and thus likely available to anyone. Especially with the sources of uncertainty accounted for, the agreement of these in situ measurements with our reconstructed SWE values and the lack of bias in our modeled values are encouraging.

3.5 Machine learning modeling

Given the size of the dataset, 104 million predictor and target observations, random subsampling was used to keep the computation times reasonable. F_{SCA} values of zero were excluded since ($F_{SCA} = 0$) $\stackrel{\text{def}}{=} (SWE = 0)$. Including predic-

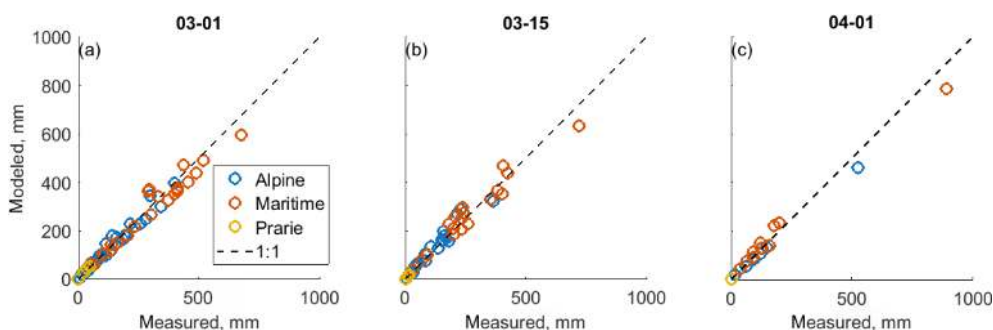


Figure 5. Model vs. measured SWE at all stations for selected dates in 2017.

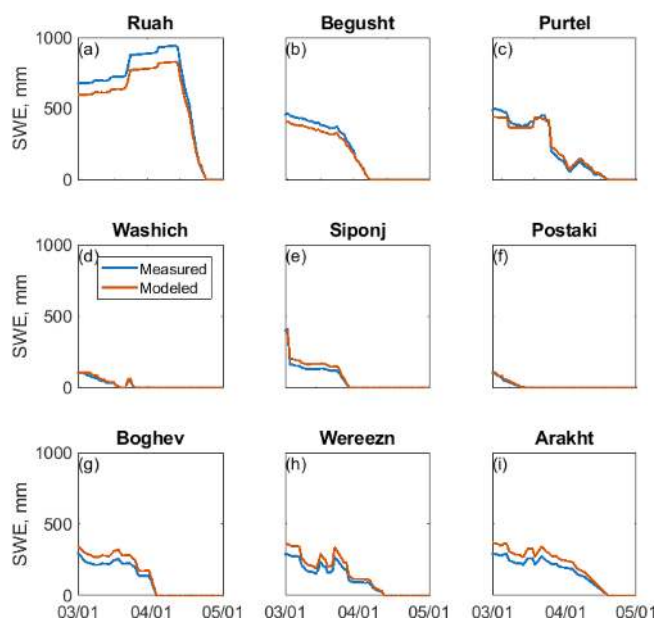


Figure 6. Model vs. measured SWE at selected AKAH stations for 2017 March to May.

tions of zero SWE would dramatically lower our error, but would imply false accuracy. At 3.125 km, about 1/3 of the pixels in the study area showed some snow or ice on every day of the year (Fig. 1, blue area). Since reconstruction cannot provide a meaningful estimate of SWE on a glacier, we also excluded those pixels from the analysis. Most of these pixels are in the Amu Darya River Basin, but some are in the Kunar Basin. April through June observations were used since reconstructed SWE estimates are valid only during ablation. Probably, some snow-covered pixels were still in the accumulation phase in early April, but most were likely melting during the day, based on the limited snow climate observations for Afghanistan. The study period could have been extended further into the summer, but was stopped at the end of June to keep the dataset size manageable. Note that the SWE reconstructions were computed over the entire 2003–2011 study period, since the SWE is built up from melt-out

backwards, but only April through June SWE estimates were used for training.

To better understand the relationships between variables, we first computed a correlation (r) matrix between the predictors and the target for 90 000 predictor and target pairs across all years (Fig. 7). Between predictors, the latitude and longitude with southwest/west distance to ocean; the southwest/west/northwest barrier difference; and the mean reconstructed SWE with F_{SCA} all had $|r| > 0.70$, indicating strong correlation. For the target reconstructed SWE, only mean reconstructed SWE and F_{SCA} had $r > 0.70$. We note that F_{SCA} was used as both a predictor and to compute the reconstructed SWE, the target. Likewise, the daily mean reconstructed SWE was computed across all years, excluding the year currently being predicted, and used as a predictor. Correlation between predictors and targets is desirable but correlation between predictors, called collinearity, is not. Collinearity does not degrade the performance of the models, but makes assessment of the importance of the correlated predictors independently more difficult (Dormann et al., 2013), an issue we address in the results.

A half-dozen different approaches were tried on randomly selected subsets of data from all years: stepwise multiple linear regression, support vector machines, cross-validated regression trees, least-squares (LS) boosted regression trees, bagged regression trees, and feed-forward neural networks. The bagged trees and feed-forward neural networks were selected for consistently producing the lowest root mean squared error (RMSE).

3.5.1 Bagged trees

Classification and regression trees (CART) comprise a supervised machine learning technique where predictors are recursively split to produce increasingly homogenous subsets of target data (Breiman et al., 1984). Classification trees are used for discrete, categorical data while regression trees are used for continuous data. This technique has been used extensively on snow-related prediction, for example in snow mapping (Rosenthal and Dozier, 1996) and avalanche forecasting (Davis et al., 1999; Peitzsch et al.,

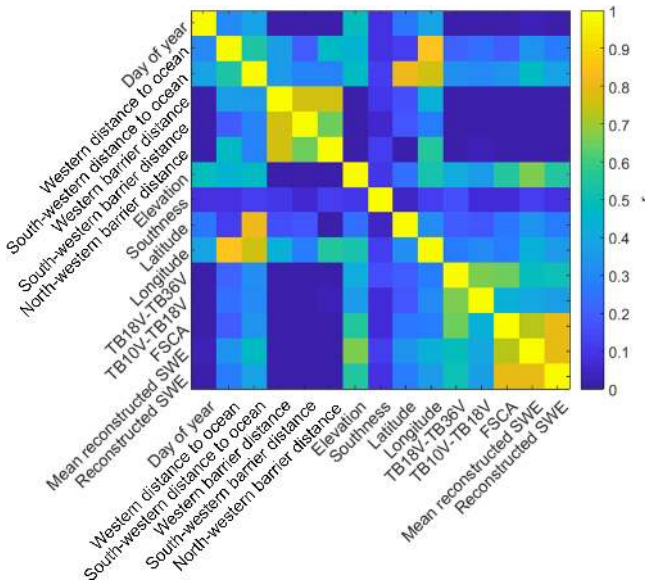


Figure 7. Correlation coefficient (r) for all variables, sampled randomly across all years.

2012), but it tends to overfit. Bagged (bootstrap-aggregated, Breiman, 1996) trees, with the most recent developments called random forests (Breiman, 2001), are ensemble methods whereby multiple trees are grown from random subsets of predictors, producing a weighted ensemble of trees. Bagged trees reduce overfitting and increase predictive accuracy over single trees (Breiman, 2001). Regression ensemble hyperparameters were optimized by minimizing cross-validation loss; the parameters included the method (i.e., bagged or LS boosted), number of learning cycles, maximum number of splits, minimum leaf size, and number of variables to randomly sample.

3.5.2 Neural networks

Neural networks attempt to mimic biological systems by creating a network of interconnected and weighted elements called neurons (Hagan et al., 2014). The neurons provide the connection between the predictors and the target. In supervised learning, the weights of the neurons are iteratively adjusted to minimize error. For our study, a feed-forward neural network was selected for simplicity. One set of parameters to optimize, the number of neurons in each hidden layer, was chosen by testing different combinations on the randomly selected subsets.

3.5.3 Training and prediction

For the final model training, each year from 2003 through 2011 was run separately. For each year, 80 000 randomly selected predictor and target observations were selected for training from all years except the current target year. The trained models were then used to predict 10 000 targets for

the target year. Larger sample sizes of 800 000 training observations were tried but did not improve model accuracy. For each basin, 90 000 randomly selected predictor and target observations were used with 20 % of the observations held out for validation. Residuals and summary error information, RMSE and bias, were stored for each year. All years were then run by basin to examine regional differences in model performance.

Bagged trees and neural networks have been referred to informally as black boxes, because the model structure is complicated and difficult or impossible to interpret, but regression trees offer the ability to independently assess predictor performance. For a single tree, estimates of predictor importance are computed by summing changes in the model mean squared error using every split for a predictor, then dividing by the total number of splits where that predictor appears (Breiman et al., 1984). This method can be repeated over all the trees in the ensemble and then averaged to obtain an ensemble predictor importance (Friedman and Meulman, 2003). We used this technique to examine predictor importance, which ranges from 0 to 1, for the bagged trees. We also tried the out-of-bag permuted predictor importance (Breiman, 2001), but found that it showed high importance for predictors not well correlated with the target. One possible explanation is that correlated predictors can be overestimated using this method (Strobl et al., 2008). Thus, we only used the predictor importance as Friedman and Meulman (2003) define.

4 Results and discussion

The bagged trees and the neural networks performed similarly when grouped by year (Fig. 8a, b). Mean bias across all years is 14 % for both methods, and RMSE values are 46 to 48 mm. Year-to-year error is similar, with errors ranging from 29 to 86 mm RMSE with -49 to $+94$ % bias for the bagged trees and 31 to 87 mm RMSE with -48 to $+88$ % bias for the neural networks. Error plots were almost identical, so only those for the slightly better performing bagged trees are shown (Fig. 8b).

The worst misses came in 2004, where both models showed high bias, and 2009, where both models were low. Those years coincide with anomalously low and high total SWE volumes, especially at the beginning of the melt season (Fig. 2). Similarly, when grouped by basin (Fig. 9a, b) the bagged trees and neural networks had nearly identical performance with mean values across all basins of 22–28 mm RMSE and 0 % bias. The RMSE ranged from 6 to 45 mm RMSE for the bagged trees and 9 to 58 mm for the neural networks. Given that the bias only ranged from 0–1 % for the bagged trees and was 0 % for the neural networks, it is clear that the higher RMSE is the result of different mean SWE in the basins. The highest RMSE occurred in the Upper Kabul

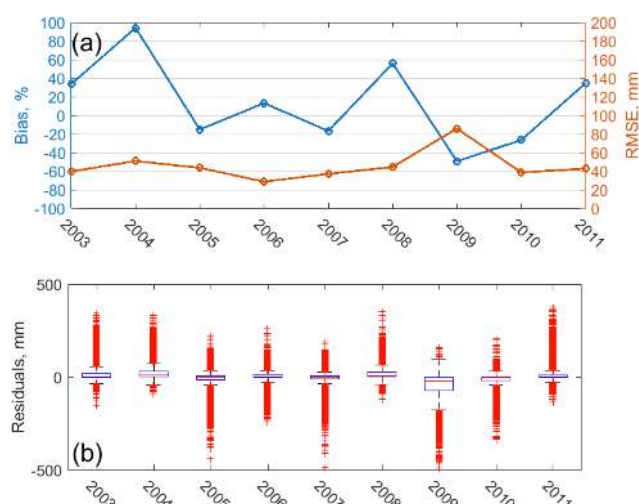


Figure 8. (a) Bagged trees bias and RMSE; (b) residuals (machine learning prediction – reconstructed SWE) by year with red line as the median, boxes encompassing the 25th (p_{25}) and 75th (p_{75}) percentiles, whiskers showing non-outlier ranges, and crosses indicating outliers, defined as points greater/less than $p_{75} \pm w$ ($p_{75} - p_{25}$), with $w = 15$.

for both models, which showed a much greater mean 1 April SWE value compared to the other basins (Table 3).

Both models showed 0 % bias for this basin, indicating excellent performance relative to the other basins. Error plots were again almost identical, so only those for the bagged trees are shown for brevity (Fig 9b).

To put these results in context, we examine performance in terms of the Nash–Sutcliffe (NS) efficiency (Nash and Sutcliffe, 1970), where the reconstructed SWE is treated as the observed result and the bagged tree/neural network SWE prediction is treated as the forecast. The NS efficiency for all years is 0.68 and ranges from 0.21 (in 2004) to 0.90 (in 2006). All years are greater than zero, indicating more skill than a mean forecast. By basin, NS efficiencies are higher averaging 0.89 and ranging from 0.87–0.91, showing that most of the forecasting challenge occurs year-to-year. Given the lack of water resources monitoring and management in Afghanistan and the high proportion of runoff from snowmelt (Daly et al., 2012; Vuyovich and Jacobs, 2011), our machine learning predictions could improve runoff predictions, which are likely based on mean conditions.

Figure 10 shows the predictor performance, ranked by importance, a relative measure ranging from 0 to 1 explained in Sect. 3.5.3. As expected, F_{SCA} and mean reconstructed SWE are by far most important predictors, with values of 0.47 and 0.26. As mentioned in Sect. 3.5, these two variables are highly correlated ($r = 0.73$) making collinearity a concern. For predictive purposes, collinearity is not an issue, but for predictor importance the collinearity means that it is not possible to separately evaluate the predictive power of F_{SCA} and mean reconstructed SWE. Clearly both are impor-

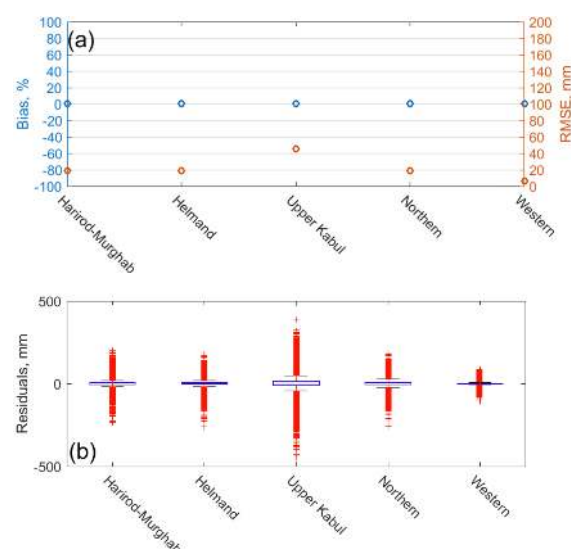


Figure 9. Same as Fig. 8, except by basin for all years, (a) Bagged trees bias and RMSE; and (b) residuals.

tant predictive variables, but F_{SCA} varies from year to year and therefore would better capture interannual variability.

All other predictors show importance < 0.08 . The third most important predictor is elevation, shown to be an important predictor in previous studies (Fassnacht et al., 2003; Fassnacht et al., 2012; Schneider and Molotch, 2016). The fourth most important variable is longitude, followed by $TB_{18V} - TB_{36V}$, the difference between microwave brightness temperatures at 18 and 36 GHz, showing that the passive microwave SWE retrievals have little predictive power.

Afghanistan is ideal for optical remote sensing, given the sparse canopy. Cloud cover is a serious limitation to optical remote sensing, but the melt season in Afghanistan is usually clear. Previous work has shown that the viewable gap fraction adjustment used here produces accurate results for under canopy snow mapping (Raleigh et al., 2013). Likewise, the lack of canopy cover in Afghanistan makes it an ideal study area for passive microwave remote sensing, but the results here are not encouraging. A detailed time series of $TB_{18V} - TB_{36V}$ and reconstructed SWE for the pixel containing Salang Pass (Fig. S3) shows the $TB_{18V} - TB_{36V}$ time series to have little year to year variability, limiting its utility for discerning wet years from dry years. The low predictive power for the passive microwave, even at the enhanced 3.125 km resolution in this ideal study area, is discouraging, although we note that the basin wide SWE volumes estimated by reconstruction were close to those estimated via passive microwave (Daly et al., 2012). However, the snow-pack was thin and much of the area in each basin was free of snow on 1 April, suggesting that the passive microwave may only be effective at mapping the presence or absence of snow rather than its depth. Given that passive microwaves are not affected by cloud cover, those data could be used to

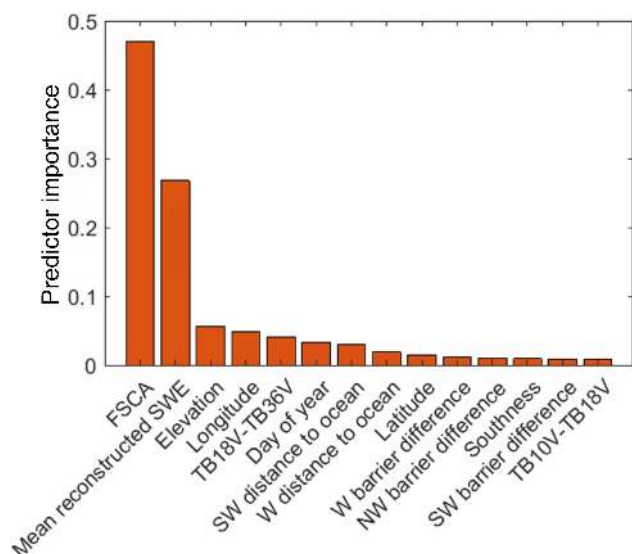


Figure 10. Predictor importance (see Sect. 3.5.3) for randomly selected observations across all years using bagged regression trees.

fill gaps caused by cloud cover in estimates of F_{SCA} derived from optical instruments.

As discussed in Sect. 3.3, our reconstructed SWE estimates are not perfect. Potential sources of uncertainty include unobservable F_{SCA} during cloudy periods, reflectance bias at higher sensor zenith angles (Dozier et al., 2008), melt out date (Slater et al., 2013), snow albedo, and wind speed. However, we assert that all of these sources of error have been vetted and addressed in depth (e.g., Bair et al., 2016; Dozier et al., 2016; Molotch et al., 2010; Rittger et al., 2016). The comparison with in situ measurements from the region are unbiased and have very low error when uncertainty is accounted for (Sect. 3.4).

These models could be implemented operationally assuming that the dynamic inputs are made available in near-real time, certainly feasible for the enhanced resolution PM brightness temperatures and for a gap-filled and smoothed MODSCAG F_{SCA} . Given the low predictor importance of the enhanced resolution PM brightness temperatures, that predictor could be excluded or substituted with a PM SWE product that is operationally available (e.g., AMSR2 SWE at 10 km resolution, Kelly, 2013). Likewise, the MODSCAG F_{SCA} is available now in near-real time from the NASA JPL Snow Data System, although it suffers from noise, gaps, and cloud–snow discrimination issues (Dozier et al., 2008). Another issue to overcome would be application of the models outside the training period, i.e., the accumulation period.

5 Conclusions

We successfully constructed two machine learning models, trained on reconstructed SWE that could be used for

operational SWE prediction in the austere watersheds of Afghanistan. We hypothesize that our reconstructed SWE estimates are the most accurate ground truth available for this region. Using novel in situ snow measurements from Afghanistan’s watersheds, we show our model to be unbiased with low errors when measurement uncertainty is accounted for. Many areas in Afghanistan show an order of magnitude more SWE than passive microwave sensors indicate. The bagged regression trees performed slightly better than the neural networks and have the added benefit of predictor importance estimates. On average over all years, the models were unbiased but over-estimated SWE in the lowest snow year and under-estimated SWE in the highest snow year. Moreover, the RMSE was higher in the basins with deeper snow, most notably the Upper Kabul, but unbiased across all basins, indicating consistent performance. Nash–Sutcliffe efficiencies average 0.68, with all years greater than zero, indicating improved skill over a mean forecast. The most important predictors were the fractional snow-covered area and the mean reconstructed SWE (excluding the year being predicted). Elevation, longitude, and a measure of SWE from the passive microwave were the third through fifth most important predictors. Our method can provide seasonal snowmelt runoff forecasts from satellite data alone, based largely on fractional snow-cover and reconstructed SWE estimates.

Data availability. Most of the data used are in government archives: calibrated passive microwave daily brightness temperatures are from the National Snow and Ice Data Center (<https://nsidc.org/pmesdr/>). MODSCAG and MODDRFS snow cover and dust radiative forcing data are from the NASA JPL Snow Data System (<https://snow.jpl.nasa.gov/portal/>). Land survey data are from the Global Land Cover Facility (<http://glcfapp.glcf.umd.edu/data/gls/>). ASTER-derived elevation grids are from the ASTER Global Digital Elevation Model (<http://dx.doi.org/10.5067/ASTER/ASTGTM.002>). The sparse climate data available collected by the World Meteorological Organization are available from the U.S. National Climatic Data Center (<ftp://ftp.atdd.noaa.gov/pub/GCOS/WMO-Normals/RA-II/AH>). GLDAS data are from NASA GSFC’s HDISC: Hydrology Data and Information Services Center (<https://disc.sci.gsfc.nasa.gov/hydrology>). CERES SYN data at 1°, 3 h resolution can be ordered at the CERES HDF Data Products page (https://ceres.larc.nasa.gov/compare_products-ed2.php). The reconstructed SWE values used as our training target dataset are available at: <ftp://ftp.snow.ucsb.edu/pub/org/snow/products/reconstruction/h23v05>.

The Supplement related to this article is available online at <https://doi.org/10.5194/tc-12-1579-2018-supplement>.

Author contributions. AAC originally began the study of machine learning for SWE reconstruction, as part of his master’s thesis, co-supervised by JD. EHB and JD subsequently carried out most of

the analyses, supported by KR's work on SWE reconstruction using MODIS and NLDAS data. EHB produced the first draft of the manuscript, which was subsequently edited by JD.

Competing interests. The authors declare that they have no conflict of interest.

Acknowledgements. This work was supported by NASA awards NNX12AJ87G and NNX15AT01G, U.S. Army Cold Regions Research and Engineering Laboratory award W913E5-16-C-0013, and an award from Microsoft Research for computing and storage on Microsoft Azure. We thank Jessica Lundquist, Steven Fassnacht, and one anonymous reviewer for their constructive comments. We are grateful to the Aga Khan Agency for Habitat for supplying snow measurements from this austere part of the world.

Edited by: Marie Dumont

Reviewed by: Steven Fassnacht, Jessica Lundquist, and one anonymous referee

References

- Adam, J. C., Clark, E. A., Lettenmaier, D. P., and Wood, E. F.: Correction of global precipitation products for orographic effects, *J. Climate*, 19, 15–38, <https://doi.org/10.1175/JCLI3604.1>, 2006.
- Bair, E. H., Dozier, J., Davis, R. E., Colee, M. T., and Clafey, K. J.: CUES – A study site for measuring snowpack energy balance in the Sierra Nevada, *Front. Earth Sci.*, 3, 58, <https://doi.org/10.3389/feart.2015.00058>, 2015.
- Bair, E. H., Rittger, K., Davis, R. E., Painter, T. H., and Dozier, J.: Validating reconstruction of snow water equivalent in California's Sierra Nevada using measurements from the NASA Airborne Snow Observatory, *Water Resour. Res.*, 52, 8437–8460, <https://doi.org/10.1002/2016WR018704>, 2016.
- Bair, E. H., Rittger, K., and Dozier, J.: Reconstructed SWE for MODIS tile h23v05, calendar years 2003–2012, data available at: <ftp://ftp.snow.ucsb.edu/pub/org/snow/products/reconstruction/h23v05>, last access: 1 June 2016.
- Barrett, A.: National Operational Hydrologic Remote Sensing Center SNOw Data Assimilation System (SNODAS) products at NSIDC, National Snow and Ice Data Center, Boulder, Special Report 11, 19, 2003.
- Beaudoin, Hiroko and M. Rodell, NASA/GSFC/HSL: GLDAS Noah Land Surface Model L4 3 hourly 0.25×0.25 degree V2.1, Greenbelt, Maryland, USA, Goddard Earth Sciences Data and Information Services Center (GES DISC), available at: <https://doi.org/10.5067/E7TYRXPJKWOQ> (last access: 1 August 2016), 2016.
- Breiman, L.: Bagging predictors, *Mach. Learn.*, 24, 123–140, <https://doi.org/10.1023/A:1018054314350>, 1996.
- Breiman, L.: Random forests, *Mach. Learn.*, 45, 5–32, <https://doi.org/10.1023/A:1010933404324>, 2001.
- Breiman, L., Friedman, J. H., Olshen, R. A., and Stone, C. J.: Classification and Regression Trees, Chapman and Hall, New York, 368 pp., 1984.
- Brodzik, M. J. and Long, D.: Calibrated Passive Microwave Daily EASE-Grid 2.0 Brightness Temperature ESDR (CETB), National Snow and Ice Data Center, Boulder, CETB ATBD rev 0.11, 91, 2016.
- Brodzik, M. J., Long, D. G., Hardman M. A., Paget, A., and Armstrong, R.: MEaSUREs Calibrated Enhanced-Resolution Passive Microwave Daily EASE-Grid 2.0 Brightness Temperature ESDR, Version 1, various resolutions, Cylindrical Equal Area Projection, Boulder, Colorado USA, NASA National Snow and Ice Data Center Distributed Active Archive Center, available at: <https://doi.org/10.5067/MEASURES/CRYOSPHERE/NSIDC-0630.001> (last access: 4 August 2017), 2016.
- Burt, P. and Adelson, E.: The Laplacian pyramid as a compact image code, *IEEE T. Commun.*, 31, 532–540, <https://doi.org/10.1109/TCOM.1983.1095851>, 1983.
- Chabot, D. and Kaba, A.: Avalanche forecasting in the central Asian countries of Afghanistan, Pakistan and Tajikistan, *Proc. 2016 Intl. Snow Sci. Wksp.*, Breckenridge, CO, available at: <http://arc.lib.montana.edu/snow-science/item/2310> (last access: 23 April 2018), 2016.
- Cosgrove, B. A., Lohmann, D., Mitchell, K. E., Houser, P. R., Wood, E. F., Schaake, J. C., Robock, A., Marshall, C., Sheffield, J., Duan, Q., Luo, L., Higgins, R. W., Pinker, R. T., Tarpley, J. D., and Meng, J.: Real-time and retrospective forcing in the North American Land Data Assimilation System (NLDAS) project, *J. Geophys. Res.-Atmos.*, 108, 8842, <https://doi.org/10.1029/2002JD003118>, 2003.
- Daly, S. F., Vuyovich, C. M., Deeb, E. J., Newman, S. D., Baldwin, T. B., and Gagnon, J. J.: Assessment of the snow conditions in the major watersheds of Afghanistan using multispectral and passive microwave remote sensing, *Hydrol. Process.*, 26, 2631–2642, <https://doi.org/10.1002/hyp.9367>, 2012.
- Davis, R. E., Elder, K., Howlett, D., and Bouzaglou, E.: Relating storm and weather factors to dry slab avalanche activity at Alta, Utah, and Mammoth Mountain, California, using classification and regression trees, *Cold Reg. Sci. Technol.*, 30, 79–89, [https://doi.org/10.1016/S0165-232X\(99\)00032-4](https://doi.org/10.1016/S0165-232X(99)00032-4), 1999.
- Derksen, C., Walker, A., and Goodison, B.: Evaluation of passive microwave snow water equivalent retrievals across the boreal forest/tundra transition of western Canada, *Remote Sens. Environ.*, 96, 315–327, <https://doi.org/10.1016/j.rse.2005.02.014>, 2005.
- Doelling, D.: CERES SYN 1 deg 3-hour edition 3A, surface fluxes, available at: [10.5067/TERRA+AQUA/CERES/SYN1DEG3HOUR_L3.003A](https://doi.org/10.5067/TERRA+AQUA/CERES/SYN1DEG3HOUR_L3.003A), last access: 17 October 2017.
- Dormann, C. F., Elith, J., Bacher, S., Buchmann, C., Carl, G., Carré, G., Marquéz, J. R. G., Gruber, B., Lafourcade, B., Leitão, P. J., Münkemüller, T., McClean, C., Osborne, P. E., Reineking, B., Schröder, B., Skidmore, A. K., Zurell, D., and Lautenbach, S.: Collinearity: A review of methods to deal with it and a simulation study evaluating their performance, *Ecography*, 36, 27–46, <https://doi.org/10.1111/j.1600-0587.2012.07348.x>, 2013.
- Dozier, J.: Mountain hydrology, snow color, and the fourth paradigm, *Eos, Transactions American Geophysical Union*, 92, 373–375, <https://doi.org/10.1029/2011EO430001>, 2011.
- Dozier, J. and Frew, J.: Rapid calculation of terrain parameters for radiation modeling from digital elevation data, *IEEE Geosci. Remote S.*, 28, 963–969, <https://doi.org/10.1109/36.58986>, 1990.

- Dozier, J., Painter, T. H., Rittger, K., and Frew, J. E.: Time-space continuity of daily maps of fractional snow cover and albedo from MODIS, *Adv. Water Resour.*, 31, 1515–1526, <https://doi.org/10.1016/j.advwatres.2008.08.011>, 2008.
- Dozier, J., Bair, E. H., and Davis, R. E.: Estimating the spatial distribution of snow water equivalent in the world's mountains, *WIREs Water*, 3, 461–474, <https://doi.org/10.1002/wat2.1140>, 2016.
- Durand, M., Kim, E. J., Margulis, S. A., and Molotch, N. P.: A first-order characterization of errors from neglecting stratigraphy in forward and inverse passive microwave modeling of snow, *IEEE Geosci. Remote S.*, 8, 730–734, <https://doi.org/10.1109/LGRS.2011.2105243>, 2011.
- Fassnacht, S. R., Dressler, K. A., and Bales, R. C.: Snow water equivalent interpolation for the Colorado River Basin from snow telemetry (SNOTEL) data, *Water Resour. Res.*, 39, 1208, <https://doi.org/10.1029/2002WR001512>, 2003.
- Fassnacht, S. R., Dressler, K. A., Hultstrand, D. M., Bales, R. C., and Patterson, G.: Temporal inconsistencies in coarse-scale snow water equivalent patterns: Colorado River Basin snow telemetry-topography regressions, *Pirineos: Revista de Ecología de Montaña*, 167, 165–185, <https://doi.org/10.3989/Pirineos.2012.167008>, 2012.
- Friedman, J. H. and Meulman, J. J.: Multiple additive regression trees with application in epidemiology, *Stat. Med.*, 22, 1365–1381, <https://doi.org/10.1002/sim.1501>, 2003.
- Giroto, M., Margulis, S. A., and Durand, M.: Probabilistic SWE reanalysis as a generalization of deterministic SWE reconstruction techniques, *Hydrol. Process.*, 28, 3875–3895, <https://doi.org/10.1002/hyp.9887>, 2014.
- Guan, B., Molotch, N. P., Waliser, D. E., Jepsen, S. M., Painter, T. H., and Dozier, J.: Snow water equivalent in the Sierra Nevada: Blending snow sensor observations with snowmelt model simulations, *Water Resour. Res.*, 49, 5029–5046, <https://doi.org/10.1002/wrcr.20387>, 2013.
- Hagan, M. T., Demuth, H. B., Beale, M. H., and De Jesús, O.: *Neural Network Design*, 2nd Edn., edited by: Hagan, M., Stillwater, OK, 800 pp., 2014.
- Hampel, F. R.: The influence curve and its role in robust estimation, *J. Am. Stat. Assoc.*, 69, 383–393, <https://doi.org/10.1080/01621459.1974.10482962>, 1974.
- Hancock, S., Baxter, R., Evans, J., and Huntley, B.: Evaluating global snow water equivalent products for testing land surface models, *Remote Sens. Environ.*, 128, 107–117, <https://doi.org/10.1016/j.rse.2012.10.004>, 2013.
- Hastie, T., Tibshirani, R., and Friedman, J.: *The Elements of Statistical Learning: Data Mining, Inference, and Prediction*, 2nd Edn., Springer, Berlin, 745 pp., 2009.
- Hinkelman, L. M., Lapo, K. E., Cristea, N. C., and Lundquist, J. D.: Using CERES SYN surface irradiance data as forcing for snowmelt simulation in complex terrain, *J. Hydrometeorol.*, 16, 2133–2152, <https://doi.org/10.1175/JHM-D-14-0179.1>, 2015.
- Jepsen, S. M., Molotch, N. P., Williams, M. W., Rittger, K. E., and Sickman, J. O.: Interannual variability of snowmelt in the Sierra Nevada and Rocky Mountains, United States: Examples from two alpine watersheds, *Water Resour. Res.*, 48, W02529, <https://doi.org/10.1029/2011WR011006>, 2012.
- Kattelmann, R.: Snowmelt lysimeters in the evaluation of snowmelt models, *Ann. Glaciol.*, 31, 406–410, <https://doi.org/10.3189/172756400781820048>, 2000.
- Kelly, R.: The AMSR-E snow depth algorithm: Description and initial results, *Journal of the Remote Sensing Society of Japan*, 29, 307–317, <https://doi.org/10.11440/rssj.29.307>, 2009.
- Kelly, R.: Descriptions of GCOM-W1 AMSR2 Level 1R and Level 2 Algorithms, Earth Observation Research Center, Japan Aerospace Exploration Agency, Report NDX-120015A, 17, 2013.
- Kelly, R. E., Chang, A. T. C., Tsang, L., and Foster, J. L.: A prototype AMSR-E global snow area and snow depth algorithm, *IEEE Geosci. Remote S.*, 41, 230–242, <https://doi.org/10.1109/TGRS.2003.809118>, 2003.
- Lapo, K. E., Hinkelman, L. M., Sumargo, E., Hughes, M., and Lundquist, J. D.: A critical evaluation of modeled solar irradiance over California for hydrologic and land surface modeling, *J. Geophys. Res.-Atmos.*, 122, 299–317, <https://doi.org/10.1002/2016JD025527>, 2017.
- Lettenmaier, D. P., Alsdorf, D., Dozier, J., Huffman, G. J., Pan, M., and Wood, E. F.: Inroads of remote sensing into hydrologic science during the WRR era, *Water Resour. Res.*, 51, 7309–7342, <https://doi.org/10.1002/2015WR017616>, 2015.
- Li, Z.-X.: Modelling the passive microwave remote sensing of wet snow, *Prog. Electromagn. Res.*, 62, 143–164, <https://doi.org/10.2528/PIER05102402>, 2006.
- Liston, G. E. and Elder, K.: A meteorological distribution system for high-resolution terrestrial modeling (MicroMet), *J. Hydrometeorol.*, 7, 217–234, <https://doi.org/10.1175/JHM486.1>, 2006.
- Liston, G. E., Haehnel, R. B., Sturm, M., Hiemstra, C. A., Berzovskaya, S., and Tabler, R. D.: Simulating complex snow distributions in windy environments using SnowTran-3D, *J. Glaciol.*, 53, 241–256, <https://doi.org/10.3189/172756507782202865>, 2007.
- Malik, M. J., van der Velde, R., Vekerdy, Z., and Su, Z.: Improving modeled snow albedo estimates during the spring melt season, *J. Geophys. Res.-Atmos.*, 119, 7311–7331, <https://doi.org/10.1002/2013JD021344>, 2014.
- Margulis, S. A., Giroto, M., Cortés, G., and Durand, M.: A particle batch smoother approach to snow water equivalent estimation, *J. Hydrometeorol.*, 16, 1752–1772, <https://doi.org/10.1175/JHM-D-14-0177.1>, 2015.
- Marks, D. and Dozier, J.: Climate and energy exchange at the snow surface in the alpine region of the Sierra Nevada, 2, Snow cover energy balance, *Water Resour. Res.*, 28, 3043–3054, <https://doi.org/10.1029/92WR01483>, 1992.
- Markstrom, S. L., Regan, R. S., Hay, L. E., Viger, R. J., Webb, R. M. T., Payn, R. A., and LaFontaine, J. H.: PRMS-IV, the precipitation-runoff modeling system, version 4: U.S. Geol. Surv. Techniques and Methods, 6, B7, 158 pp., 2015.
- Markus, T., Powell, D. C., and Wang, J. R.: Sensitivity of passive microwave snow depth retrievals to weather effects and snow evolution, *IEEE Geosci. Remote S.*, 44, 68–77, <https://doi.org/10.1109/TGRS.2005.860208>, 2006.
- Martinec, J. and Rango, A.: Areal distribution of snow water equivalent evaluated by snow cover monitoring, *Water Resour. Res.*, 17, 1480–1488, <https://doi.org/10.1029/WR017i005p01480>, 1981.
- Milly, P. C. D. and Dunne, K. A.: Macroscale water fluxes 1. Quantifying errors in the estimation of basin mean precipitation, *Water*

- Resour. Res., 38, 1205, <https://doi.org/10.1029/2001WR000759>, 2002.
- Molotch, N. P.: Reconstructing snow water equivalent in the Rio Grande headwaters using remotely sensed snow cover data and a spatially distributed snowmelt model, *Hydrol. Process.*, 23, 1076–1089, <https://doi.org/10.1002/hyp.7206>, 2009.
- Molotch, N. P. and Bales, R. C.: Scaling snow observations from the point to the grid element: Implications for observation network design, *Water Resour. Res.*, 41, W11421, <https://doi.org/10.1029/2005WR004229>, 2005.
- Molotch, N. P. and Bales, R. C.: Comparison of ground-based and airborne snow surface albedo parameterizations in an alpine watershed: Impact on snowpack mass balance, *Water Resour. Res.*, 42, W05410, <https://doi.org/10.1029/2005WR004522>, 2006.
- Molotch, N. P. and Margulis, S. A.: Estimating the distribution of snow water equivalent using remotely sensed snow cover data and a spatially distributed snowmelt model: A multi-resolution, multi-sensor comparison, *Adv. Water Resour.*, 31, 1503–1514, <https://doi.org/10.1016/j.advwatres.2008.07.017>, 2008.
- Molotch, N. P., Margulis, S. A., and Jepsen, S. M.: Response to comment by A.G. Slater, M.P. Clark, and A.P. Barrett on “Estimating the distribution of snow water equivalent using remotely sensed snow cover data and a spatially distributed snowmelt model: A multi-resolution, multi-sensor comparison” [*Adv. Water Resour.*, 31, 1503–1514, 2008]. *Adv. Water Resour.*, 32, 1680–1684, 2009]. *Adv. Water Resour.*, 33, 231–239, <https://doi.org/10.1016/j.advwatres.2009.11.008>, 2010.
- NASA/METI/AIST/Japan Spacesystems and U.S./Japan ASTER Science Team: ASTER Global Digital Elevation Model, various tiles, NASA EOSDIS Land Processes DAAC, available at: <https://doi.org/10.5067/ASTER/ASTGTM.002> (last access: 4 December 2014), 2009.
- Nash, J. E. and Sutcliffe, J. V.: River flow forecasting through conceptual models part I – A discussion of principles, *J. Hydrol.*, 10, 282–290, [https://doi.org/10.1016/0022-1694\(70\)90255-6](https://doi.org/10.1016/0022-1694(70)90255-6), 1970.
- Nolin, A. W.: Recent advances in remote sensing of seasonal snow, *J. Glaciol.*, 56, 1141–1150, <https://doi.org/10.3189/002214311796406077>, 2010.
- Painter, T. H., Rittger, K., McKenzie, C., Slaughter, P., Davis, R. E., and Dozier, J.: Retrieval of subpixel snow-covered area, grain size, and albedo from MODIS, *Remote Sens. Environ.*, 113, 868–879, <https://doi.org/10.1016/j.rse.2009.01.001>, data available at: <https://snow.jpl.nasa.gov> (last access: 23 March 2017), 2009.
- Painter, T. H., Bryant, A. C., and Skiles, S. M.: Radiative forcing by light absorbing impurities in snow from MODIS surface reflectance data, *Geophys. Res. Lett.*, 39, L17502, <https://doi.org/10.1029/2012GL052457>, 2012a.
- Painter, T. H., Brodzik, M. J., Racoviteanu, A., and Armstrong, R.: Automated mapping of Earth’s annual minimum exposed snow and ice with MODIS, *Geophys. Res. Lett.*, 39, L20501, <https://doi.org/10.1029/2012GL053340>, 2012b.
- Peitzsch, E. H., Hendriks, J., Fagre, D. B., and Reardon, B.: Examining spring wet slab and glide avalanche occurrence along the Going-to-the-Sun Road corridor, Glacier National Park, Montana, USA, *Cold Reg. Sci. Technol.*, 78, 73–81, <https://doi.org/10.1016/j.coldregions.2012.01.012>, 2012.
- Raleigh, M. S., Rittger, K., Moore, C. E., Henn, B., Lutz, J. A., and Lundquist, J. D.: Ground-based testing of MODIS fractional snow cover in subalpine meadows and forests of the Sierra Nevada, *Remote Sens. Environ.*, 128, 44–57, <https://doi.org/10.1016/j.rse.2012.09.016>, 2013.
- Rittger, K., Painter, T. H., and Dozier, J.: Assessment of methods for mapping snow cover from MODIS, *Adv. Water Resour.*, 51, 367–380, <https://doi.org/10.1016/j.advwatres.2012.03.002>, 2013.
- Rittger, K., Bair, E. H., Kahl, A., and Dozier, J.: Spatial estimates of snow water equivalent from reconstruction, *Adv. Water Resour.*, 94, 345–363, <https://doi.org/10.1016/j.advwatres.2016.05.015>, 2016.
- Rodell, M., Houser, P. R., Jambor, U., Gottschalck, J., Mitchell, K., Meng, C. J., Arsenault, K., Cosgrove, B., Radakovich, J., Bosilovich, M., Entin, J. K., Walker, J. P., Lohmann, D., and Toll, D.: The Global Land Data Assimilation System, *B. Am. Meteor. Soc.*, 85, 381–394, <https://doi.org/10.1175/BAMS-85-3-381>, 2004.
- Rosenthal, W. and Dozier, J.: Automated mapping of montane snow cover at subpixel resolution from the Landsat Thematic Mapper, *Water Resour. Res.*, 32, 115–130, <https://doi.org/10.1029/95WR02718>, 1996.
- Rutan, D. A., Kato, S., Doelling, D. R., Rose, F. G., Nguyen, L. T., Caldwell, T. E., and Loeb, N. G.: CERES synoptic product: Methodology and validation of surface radiant flux, *J. Atmos. Ocean. Technol.*, 32, 1121–1143, <https://doi.org/10.1175/JTECH-D-14-00165.1>, 2015.
- Schneider, D. and Molotch, N. P.: Real-time estimation of snow water equivalent in the Upper Colorado River Basin using MODIS-based SWE reconstructions and SNOTEL data, *Water Resour. Res.*, 52, 7892–7910, <https://doi.org/10.1002/2016WR019067>, 2016.
- Schulz, O. and de Jong, C.: Snowmelt and sublimation: field experiments and modelling in the High Atlas Mountains of Morocco, *Hydrol. Earth Syst. Sci.*, 8, 1076–1089, <https://doi.org/10.5194/hess-8-1076-2004>, 2004.
- Slater, A. G., Barrett, A. P., Clark, M. P., Lundquist, J. D., and Raleigh, M. S.: Uncertainty in seasonal snow reconstruction: Relative impacts of model forcing and image availability, *Adv. Water Resour.*, 55, 165–177, <https://doi.org/10.1016/j.advwatres.2012.07.006>, 2013.
- Strobl, C., Boulesteix, A.-L., Kneib, T., Augustin, T., and Zeileis, A.: Conditional variable importance for random forests, *BMC Bioinformatics*, 9, 307, <https://doi.org/10.1186/1471-2105-9-307>, 2008.
- Sturm, M., Holmgren, J., and Liston, G. E.: A seasonal snow cover classification system for local to global applications, *J. Climate*, 8, 1261–1283, [https://doi.org/10.1175/1520-0442\(1995\)008<1261:ASSCCS>2.0.CO;2](https://doi.org/10.1175/1520-0442(1995)008<1261:ASSCCS>2.0.CO;2), 1995.
- Sturm, M., Taras, B., Liston, G. E., Derksen, C., Jonas, T., and Lea, J.: Estimating snow water equivalent using snow depth data and climate classes, *J. Hydrometeorol.*, 11, 1380–1394, <https://doi.org/10.1175/2010jhm1202.1>, 2010.
- Takala, M., Luojus, K., Pulliainen, J., Derksen, C., Lemmetyinen, J., Kärnä, J.-P., Koskinen, J., and Bojkov, B.: Estimating Northern Hemisphere snow water equivalent for climate research through assimilation of space-borne radiometer data and ground-based measurements, *Remote Sens. Environ.*, 115, 3517–3529, <https://doi.org/10.1016/j.rse.2011.08.014>, 2011.
- Tan, B., Woodcock, C. E., Hu, J., Zhang, P., Ozdogan, M., Huang, D., Yang, W., Knyazikhin, Y., and Myneni, R. B.: The impact of gridding artifacts on the local spatial properties of MODIS

- data: Implications for validation, compositing, and band-to-band registration across resolutions, *Remote Sens. Environ.*, 105, 98–114, <https://doi.org/10.1016/j.rse.2006.06.008>, 2006.
- Tedesco, M. and Narvekar, P. S.: Assessment of the NASA AMSR-E SWE product, *IEEE J. Sel. Top. Appl.*, 3, 141–159, <https://doi.org/10.1109/JSTARS.2010.2040462>, 2010.
- United Nations: UNEP in Afghanistan: Laying the foundations for sustainable development, United Nations Environment Programme, Geneva, 36, 2009.
- USAID: Afghanistan Food Security Update, FEWS Net, Washington, DC, 4, 2008.
- USGS: Global Land Survey, available at: <http://glcfapp.glcf.umd.edu/data/gls/> (last access: 1 September 2017), 2009.
- US Army Corps of Engineers: Snow Hydrology: Summary Report of the Snow Investigations, North Pacific Division, Corps of Engineers, Portland, OR, 462 pp., 1956.
- Vander Jagt, B. J., Durand, M. T., Margulis, S. A., Kim, E. J., and Molotch, N. P.: The effect of spatial variability on the sensitivity of passive microwave measurements to snow water equivalent, *Remote Sens. Environ.*, 136, 163–179, <https://doi.org/10.1016/j.rse.2013.05.002>, 2013.
- Vuyovich, C. and Jacobs, J. M.: Snowpack and runoff generation using AMSR-E passive microwave observations in the Upper Helmand Watershed, Afghanistan, *Remote Sens. Environ.*, 115, 3313–3321, <https://doi.org/10.1016/j.rse.2011.07.014>, 2011.
- Warren, S. and Wiscombe, W.: A model for the spectral albedo of snow, II, Snow containing atmospheric aerosols, *J. Atmos. Sci.*, 37, 2734–2745, [https://doi.org/10.1175/1520-0469\(1980\)037<2734:AMFTSA>2.0.CO;2](https://doi.org/10.1175/1520-0469(1980)037<2734:AMFTSA>2.0.CO;2), 1980.
- Wever, N., Fierz, C., Mitterer, C., Hirashima, H., and Lehning, M.: Solving Richards Equation for snow improves snowpack melt-water runoff estimations in detailed multi-layer snowpack model, *The Cryosphere*, 8, 257–274, <https://doi.org/10.5194/tc-8-257-2014>, 2014.
- World Meteorological Organization: 1961–1990 Global climate normals, available at: <ftp://ftp.atdd.noaa.gov/pub/GCOS/WMO-Normals/RA-II/AH> (last access: 28 August 2017), 1998.
- Xia, Y., Mitchell, K., Ek, M., Sheffield, J., Cosgrove, B., Wood, E., Luo, L., Alonge, C., Wei, H., Meng, J., Livneh, B., Lettenmaier, D., Koren, V., Duan, Q., Mo, K., Fan, Y., and Mocko, D.: Continental-scale water and energy flux analysis and validation for the North American Land Data Assimilation System project phase 2 (NLDAS-2): 1. Intercomparison and application of model products, *J. Geophys. Res.-Atmos.*, 117, D03109, <https://doi.org/10.1029/2011JD016048>, 2012.
- Xiaoxiong, X., Nianzeng, C., and Barnes, W.: Terra MODIS on-orbit spatial characterization and performance, *IEEE Geosci. Remote S.*, 43, 355–365, <https://doi.org/10.1109/TGRS.2004.840643>, 2005.